Behavior of a particle-laden flow in a spiral channel

Sungyon Lee,[1,2] Yvonne Stokes,[3,*] and Andrea L. Bertozzi[1,†]

[1]*Dept. of Mathematics and Applied Mathematics Laboratory, University of California, Los Angeles, CA 90095, USA*

[2]*Dept. of Mechanical Engineering, Texas A&M, College Station, TX 77843, USA*

[3]*School of Mathematical Sciences, The University of Adelaide, South Australia, 5005, Australia*

(Dated: September 15, 2013)

Abstract

Spiral gravity separators are devices used in mineral processing to separate particles based on their specific gravity or size. The spiral geometry allows for the simultaneous application of gravitational and centripetal forces on the particles, which leads to segregation of particles. However, this segregation mechanism is not fundamentally understood, and the spiral separator literatures does not tell a cohesive story either experimentally or theoretically. While experimental results vary depending on the specific spiral separator used, present theoretical works neglect the significant coupling between the particle dynamics and the flow field. Using work on gravity-driven monodisperse slurries on an incline that empirically accounts for this coupling, we consider a monodisperse particle slurry of small depth flowing down a rectangular channel that is helically wound around a vertical axis. We use a thin-film approximation to derive an equilibrium profile for the particle concentration and fluid depth and find that, in the steady state limit, the particles concentrate towards the vertical axis of the helix, leaving a region of clear fluid.

*Electronic address: yvonne.stokes@adelaide.edu.au

†Electronic address: bertozzi@math.ucla.edu

I. INTRODUCTION

Multiphase flows are commonplace in the surrounding environment and in numerous industrial processes and improved understanding of them will yield significant benefits. Mechanisms for segregation of solid-liquid and liquid-liquid mixtures have important applications in mining, water purification, bio-fuel generation and oil spill clean-up. Motivated by spiral particle separators, used primarily by the mineral and coal processing industries [1, 2], in this paper we consider the behavior of a slurry of fluid and particles in a helically wound channel (see Figure 1).

Mined minerals undergo processing to be extracted from the gangue. Amongst different mineral processing methods, the spiral separator stands out as one of the most economical devices for segregating solid particles in a slurry because of their simplicity and robustness. It is a helically-wound channel along which a particle-laden slurry flows under gravity. Like in curved pipes [3], there is a primary flow along the channel and, because of the curvature of the channel, a secondary flow in the cross section plane normal to the channel axis. It is this secondary flow which acts to segregate particles by size/density [4]. Although used in the mining industry since the 1940's, their design has been largely based on trial and error, rather than fundamental understanding of the physics at hand. A number of theoretical and experimental studies have been done to remedy this. Holland-Batt and Holtham [2] experimentally demonstrated the presence of the secondary flow normal to the axial direction, using a clear fluid feed and a dye for flow visualization. They also showed, for a feed containing tracer particles of constant density and of three different sizes, that particles of different sizes exit the separator at different radial positions which depend on both the separator geometry and the flow rate. However, there is clear lack of understanding of the fundamental physics, which is essential for the design and evaluation of spiral separators [5]. The aim of this paper is to address this lack.

A few theoretical investigations have been undertaken on the fluid dynamics in the spiral channel. Most recently, Stokes et al. [6, 7] derived a new model for helically-symmetric clear-fluid flow in the thin film limit which yields the primary and secondary flows, along with the free surface shape. Das et al. [8] considered a particle-laden flow in a spiral separator and applied the particle dispersion model of Bagnold [9], showing that the particles of a larger relative gravity accumulate toward the center of the spiral. In their analysis, however,

the viscosity and density of the mixture are constant, independent of the local particle concentration. Matthews et al. [10] conducted full CFD simulations of flow in an industrial separator and then computed the trajectories of individual particles in the flow. In this work, the fluid flow is assumed to be completely undisturbed by the particles, which again removes the coupling between the flow and the particles.

In more recent years, considerable work has been done on monodisperse particle-laden flows down inclined planes with the aim of describing the coupling between fluid and particles [11–15]. Experimental studies [11, 13, 14] have showed that, even at relatively modest volume fractions of particles, the presence of the particles affects the flow, and the mixture exhibits different dynamics depending on the volume fraction. They found that the particles are subject to two physical effects: sedimentation due to gravity and shear-induced migration which opposes settling. The latter was first discovered by Leighton and Acrivos [16] and signifies that particles in concentrated suspensions undergo irreversible interactions, drifting from regions of high to low particle concentration, as well as from high to low shear stress. Mathematical models of this behavior have been developed based on a diffusive flux phenomenology [16, 17]. Cook [12] developed an equilibrium model that accounts for the interplay of particle sedimentation and shear-induced migration. Building on that, Murisic et al. [15] developed a dynamical model for relatively low particle volume fractions and showed remarkable agreement with the experiments.

The current empirical monodisperse models are more tractable than the rigorous Stokesian-dynamics model of Nott and Brady [18] and have been validated experimentally in the thin viscous-flow regime. Lee et al. [19] presented a first-attempt at extending this empirical equilibrium model to a helically-wound channel in the small-torsion limit. At steady state and with constant torsion across the channel width, the domain is split into an outer clear-fluid region and an inner region of constant particle concentration. We here build on that work and consider helically-wound channels of rectangular cross section with small centerline slope. Since spiral separators typically have small slope, this assumption is justifiable. The question we seek to answer is: "Can particles segregate out of the mixture when a slurry flows in a helically-wound channel of small slope, in the laminar *thin* film limit?" This is the natural starting point for explaining the segregation mechanism observed in spiral separators, while limiting ourselves to the flow regime that is appropriate for the current diffusive model. As in work on clear-fluid flow in helical pipes and channels [7, 20],

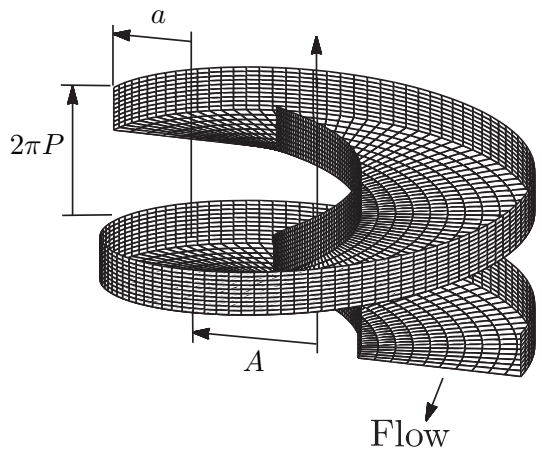

FIG. 1: A helical channel of rectangular cross section of width $2a$. The spiral radius is A, while the vertical spacing between each turn is the pitch $2\pi P$.

we assume a helically-symmetric flow, i.e. that the flow is independent of axial position along the channel and depends only on position in the two-dimensional cross section.

This paper is organized as follows. In Section II, we introduce the helical coordinates and governing equations for the fluid-particle mixture. In Sec III, the equilibrium model is derived by applying lubrication approximations in a small-slope limit. Then in IV, we uncover the segregation mechanism of the particles from the fluid in the steady state limit. We conclude the paper in V by summarizing our results and discussing future directions.

II. PROBLEM FORMULATION

We consider a mixture of particles of diameter d and a viscous liquid flowing down a helically-wound channel whose central axis is a vertical right-handed helix with radius A and pitch $2\pi P$. The channel has a rectangular cross-section of width $2a$, as shown in Figure 1. As in Manoussaki and Chadwick [21], the position of the fluid element in the helical channel is defined uniquely by three independent variables, (β, r, z), where the azimuthal coordinate β increases counterclockwise from the reference direction and is projected onto the bottom of the helical channel, r is the radial location from the axis of the helix, and z is the vertical distance from the bottom of the channel (Figure 2). We have derived the governing equations in terms of (β, r, z) and non-orthogonal basis vectors $(\mathbf{e}_\beta, \mathbf{e}_r, \mathbf{e}_z)$, using tensor calculus. Helical symmetry has been assumed so that the flow is independent of the

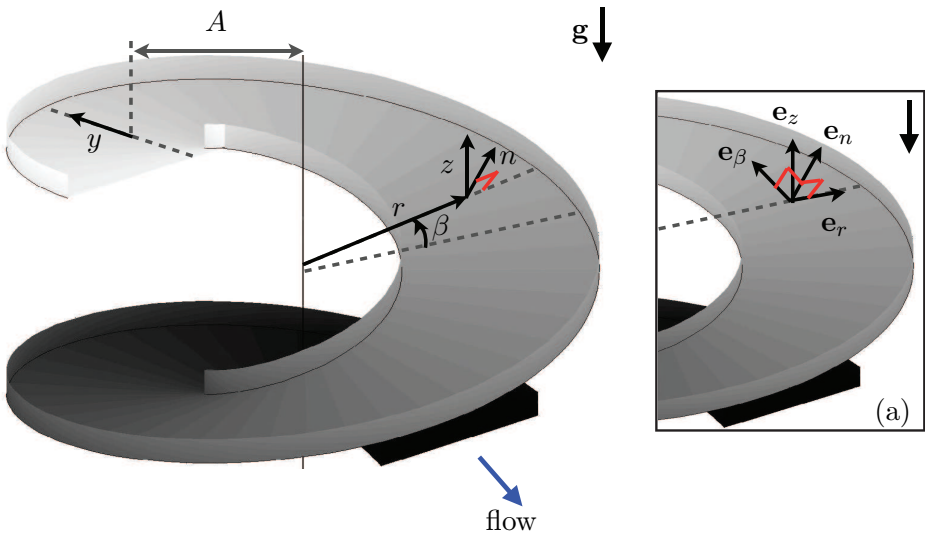

FIG. 2: Independent variables (β, r, z) are used to mark the position inside the particle-fluid mixture in the spiral channel, while the variable n (normal to the bottom of the channel) is also shown. Another radial variable y is defined from the central axis of the rectangular channel, so that $r = A + y$. The inset **(a)** shows the non-orthogonal basis vectors $(\mathbf{e}_\beta, \mathbf{e}_r, \mathbf{e}_z)$ that are used to derive the governing equations, as well as the orthogonal unit basis vectors, $(\hat{\mathbf{e}}_\beta, \hat{\mathbf{e}}_r, \hat{\mathbf{e}}_n)$.

azimuthal angle β, and all quantities are functions of r and z only. The governing equations have then been obtained in the directions of the orthogonal unit vectors $(\hat{\mathbf{e}}_\beta, \hat{\mathbf{e}}_r, \hat{\mathbf{e}}_n)$, where the unit vector $\hat{\mathbf{e}}_n = \hat{\mathbf{e}}_r \times \hat{\mathbf{e}}_\beta$ is normal to the bottom of the channel, by noting that $\mathbf{e}_z = (P\hat{\mathbf{e}}_\beta + r\hat{\mathbf{e}}_n)/\sqrt{r^2 + P^2}$. The independent variable in the direction $\hat{\mathbf{e}}_n$ is defined by $n = zr/\sqrt{r^2 + P^2}$, so that n is the distance normal to the bottom of the channel. See the Appendix for further details.

By taking the limit of $(d/H) \ll 1$, where H is the characteristic film thickness, the particles in the fluid are modeled as a continuum and are defined by a local volume fraction, ϕ. Based on the diffusive flux phenomenology, the particle-fluid mixture is modeled as an incompressible Newtonian fluid, with the density and viscosity modified by the presence of particles. The motion of the fluid-particle mixture is governed by the Cauchy momentum equations:

$$\rho(\phi)\left(\partial_t \mathbf{u} + \mathbf{u}\cdot\nabla\mathbf{u}\right) = \nabla\cdot\left(-p\mathbb{I} + \mu(\phi)(\nabla\mathbf{u} + \nabla\mathbf{u}^\top)\right) + \rho(\phi)\mathbf{g}, \tag{1}$$

and continuity, such that $\nabla\cdot\mathbf{u} = 0$. Here $\mathbf{u}$ and p are the velocity vector and pressure,

respectively, while $\mathbf{g}$ denotes the gravitational acceleration. The effect of the particles comes in through the effective viscosity μ and density ρ, which depend on ϕ [14, 15]:

$$\mu(\phi) = \mu_\ell \left(1 - \frac{\phi}{\phi_\mathrm{m}}\right)^{-2}, \qquad \rho(\phi) = \rho_p \phi + \rho_\ell (1 - \phi), \tag{2}$$

where ϕ_m refers to the maximum volume fraction, μ_ℓ and ρ_ℓ are the constant liquid viscosity and density, respectively, while ρ_p is the particle density, and $\rho_p > \rho_\ell$. On the channel walls, the velocity must vanish to satisfy the no-slip condition: $\mathbf{u} = \mathbf{0}$. On the free surface $F(r, z) = 0$, the stresses are set to zero both in normal and tangential directions, as surface tension effects are neglected: $\mathbf{n} \cdot \left(-p\mathbb{I} + \mu(\phi)(\nabla\mathbf{u} + \nabla\mathbf{u}^\top)\right) = \mathbf{0}$. The free surface is also governed by the kinematic condition: $\mathbf{n} \cdot \mathbf{u} = 0$.

Coupled with the momentum equations are two conservation equations, one for conservation of the mixture,

$$\partial_t \rho(\phi) + \nabla \cdot (\rho(\phi)\mathbf{u}) = 0, \tag{3}$$

and one for conservation of particulate material,

$$\partial_t \phi + \mathbf{u} \cdot \nabla\phi + \nabla \cdot \mathbf{J} = 0, \tag{4}$$

where $\mathbf{J}$ is the particle flux vector. There is no flux of particles through the free surface, so that $\mathbf{n} \cdot \mathbf{J} = 0$. The particle transport equation (4) consists of the convection due to flow and the diffusive term. We assume that the diffusive particle flux $\mathbf{J}$ is given by [12, 14, 15, 22]:

$$\mathbf{J} = \frac{d^2\phi(\rho_p - \rho_\ell)}{18\mu}(1 - \phi)\mathbf{g} - \frac{K_c d^2}{4}\phi\nabla(\dot{\gamma}\phi) - \frac{K_v d^2}{4}\frac{\phi^2\dot{\gamma}}{\mu(\phi)}\frac{d\mu}{d\phi}\nabla\phi, \tag{5}$$

where K_c and K_v are empirically determined diffusivities in the presence of shear, and $\dot{\gamma} = \frac{1}{4}\|\nabla\mathbf{u} + \nabla\mathbf{u}^\top\|$ is the shear rate. This expression is strictly valid in the limit of a large Péclet number, $Pe = \dot{\gamma}d^2/D \gg 1$, where D is the solvent diffusivity, and the Brownian diffusion of particles can be neglected relative to the particle diffusion due to shear. The first term in $\mathbf{J}$ corresponds to particle sedimentation due to gravity. The last two terms collectively make up the shear-induced migration [16, 17], which refers to the tendency of particles in shear to move from the areas of high to low shear stress. In contrast to the sedimentation term that describes settling of particles on the bottom of the channel, particles tend to aggregate away from the wall towards the free surface under the effects of shear-induced migration. Depending on which effect dominates, particle-laden flow experiments

[14] show that particles may reach a settled regime (*i.e.* sedimentation dominates) or a ridged regime (*i.e.* shear-induced migration dominates). The experimental results are summarized on a phase separation diagram in Figure 3 and will be discussed further in Section IV.

III. EQUILIBRIUM THIN-FILM MODEL

Based on a characteristic axial velocity U_0, the channel half-width a, and a characteristic film height H, we non-dimensionalize the variables as follows:

$$(\beta, \widehat{r}, \widehat{n}) = \left(\beta, \frac{r}{a}, \frac{n}{a\delta}\right), \quad \widehat{\mathbf{u}} = \frac{1}{U_0}\left(u, \frac{v}{\delta}, \frac{w}{\delta^2}\right), \quad \widehat{p} = \frac{Re\delta}{\rho_\ell U_0^2} p, \tag{6}$$

where $Re = \rho_\ell U_0 a/\mu_\ell$ is the Reynolds number, and $\delta \equiv H/a \ll 1$, since the flow is, typically, of small depth relative to the channel half-width. For clarity, all dimensionless quantities are denoted with hats. The spiral geometric parameters A and P are scaled by the half-width a: $\widehat{A} = A/a$, and $\widehat{P} = P/a$. The slope of the channel is defined by $\lambda = \widehat{P}/\widehat{A}$, while the dimensionless curvature and torsion are $\epsilon = \widehat{A}/(\widehat{A}^2 + \widehat{P}^2)$ and $\tau = \widehat{P}/(\widehat{A}^2 + \widehat{P}^2)$, respectively. In this paper, we consider channels with small slope such that $\lambda^2 = (\widehat{P}/\widehat{A})^2 \ll 1$, and, in this limit, the curvature and torsion are $\epsilon = 1/\widehat{A}$ and $\tau = \widehat{P}/\widehat{A}^2 = \epsilon\lambda$. Physically, $\lambda^2 \ll 1$ signifies helical channels that are compressed in the vertical direction so that the vertical rise in one turn (i.e. the pitch $2\pi P$) is sufficiently small compared with the arc-length distance $2\pi A$. The effective dimensionless density $\widehat{\rho}(\phi)$ and viscosity $\widehat{\mu}(\phi)$ are scaled by ρ_ℓ and μ_ℓ, respectively. Furthermore, we define $\widehat{r} = \widehat{A} + \widehat{y}$, so that the new dimensionless radial coordinate $\widehat{y}$ is defined from the centerline of the rectangular channel, and $-1 \le \widehat{y} \le 1$. The local inclination angle of the channel is defined as $\alpha(\widehat{y}) = \arctan(\lambda/(1+\epsilon\widehat{y}))$, or $\alpha(\widehat{y}) = \arcsin(\lambda/(1+\epsilon\widehat{y}))$ in the small slope limit of $\lambda^2 \to 0$. The hats over the dimensionless quantities will be subsequently dropped for brevity.

We now simplify the momentum and particle transport equations by perturbation expansions in terms of λ and δ. To leading order, the model is

$$\frac{\partial}{\partial y}((1+\epsilon y)v) + \frac{\partial}{\partial n}((1+\epsilon y)w) = 0, \tag{7a}$$

$$\frac{\partial p}{\partial n} + \rho\kappa = 0, \quad \kappa = \frac{\delta^2 Re}{Fr^2}, \tag{7b}$$

$$\frac{\rho\kappa\lambda}{1+\epsilon y}+\frac{\partial\sigma}{\partial n}=0, \quad \sigma=\mu(\phi)\frac{\partial u}{\partial n}, \tag{7c}$$

$$-\frac{\partial p}{\partial y}-\frac{\epsilon\lambda\sigma}{(1+\epsilon y)^2}+\frac{\partial}{\partial n}\left(\mu\frac{\partial v}{\partial n}\right)+\frac{\rho\chi}{1+\epsilon y}u^2=0, \tag{7d}$$

where $Fr = U_0/\sqrt{ga}$ is the Froude number, and $\chi = \epsilon\delta Re$ is a scaled Dean number. The boundary conditions are $u = v = w = 0$ on the channel wall ($n = 0$), and, on the free surface $n = h(y)$: $\partial u/\partial n = 0$, $\partial v/\partial n = 0$, $p = 0$, and $w = v(dh/dy)$.

The crucial element in this analysis is the scaling of the particle transport equation that describes the fast equilibrium of particles in the direction normal to the channel bottom [15]. Therefore, analogous to the incline problem, we require that $\delta \ll (d/H)^2 \ll 1$, which ensures that the particle size satisfies the continuum model ($d \ll H$) without reaching a colloidal limit. The resultant rescaled particle transport equation (4) then reduces to $\partial J^n/\partial n = 0$, where J^n is the component of the particle flux in direction $\hat{\mathbf{e}}_n$, normal to the bottom of the channel. Integrating it once subject to $J^n(n = h) = 0$ yields $J^n = 0$ for all $0 \le n \le h(y)$, or

$$0=\frac{2\rho_s\kappa}{9K_c}(1-\phi)+\phi\frac{\partial\sigma}{\partial n}+\left[1+2\left(\frac{K_v-K_c}{K_c}\right)\left(\frac{\phi}{\phi_{\mathrm{m}}-\phi}\right)\right]\sigma\frac{\partial\phi}{\partial n}, \tag{8}$$

where the dimensionless density ratio ρ_s is defined as $(\rho_p - \rho_\ell)/\rho_\ell$.

IV. CONDITION FOR STEADY-STATE SOLUTION

Equations (7c) and (8) are solved simultaneously at each horizontal position y for the depth-averaged volume fraction of particles $\phi_0(y) = \int_0^1 \phi(n, y)d\widetilde{n}$, where $\widetilde{n} = n/h(y)$. This results in the expression of ϕ as an explicit function of $\widetilde{n}$, which corresponds exactly to the inclined plane problem [12]. Figure 3(a) shows examples of $\phi(\widetilde{n})$ for varying values of $\phi_0(y)$ at the channel inclination angle of $\alpha = 30^{\mathrm{o}}$. This inclination angle at $y = 0$ corresponds to setting $\lambda = P/A = 1/\sqrt{3}$. For small $\phi_0(y)$, sedimentation effects dominate, causing the particles to rapidly settle to the channel wall (*settled* regime). In this regime, ϕ is monotone decreasing in $\widetilde{n}$. When the shear-induced migration dominates for large $\phi_0(y)$ (*ridged* regime), more particles collect near the free surface, and ϕ is monotone increasing in $\widetilde{n}$. *Note that there exists a specific value of $\phi_0(y)$ such that the particle concentration is constant (i.e. $\phi = \phi_c$) in the $\widetilde{n}$ direction.* This critical volume fraction ϕ_c depends on the local channel inclination angle α and qualitatively matches the experimental results of [14],

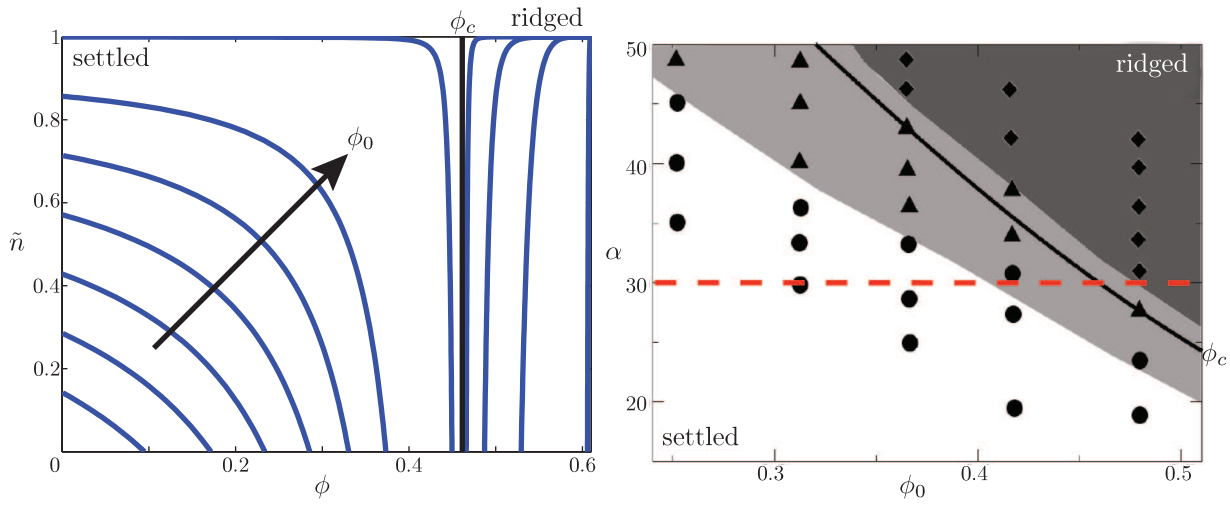

FIG. 3: **(a)** At the inclination angle of $\alpha = 30^o$, the profile of ϕ in $\widetilde{n} = n/h(y)$ is computed for increasing values of $\phi_0(y) = \int_0^1 \phi(\widetilde{n}, y)d\widetilde{n}$; the critical volume fraction ϕ_c (constant in $\widetilde{n}$) is equal to 0.461. In the spiral geometry, $\alpha = 30^o$ at $y = 0$ corresponds to setting $\lambda = 1/\sqrt{3}$. **(b)** The experimental phase diagram from [14] shows three different regimes as a function of α and ϕ_0: settled (white region, dots), transient (grey region, triangles), and ridged (darker grey, diamonds). The solid line on the phase digram is the theoretical prediction of ϕ_c which sits in the transient regime, and the dotted line highlights the angle $\alpha = 30^o$ from **(a)**.

as the value of ϕ_c sits inside the transient area between the settled and ridged regimes in the phase diagram of Figure 3(b).

The steady state solution for the particle-laden flow requires zero net flux in the y-direction, both for the fluid and solid phases, such that $\int_0^{h(y)} v(y,n)dn = 0$ and $\int_0^{h(y)} v(y,n)\phi(y,n)dn = 0$, respectively. Given $v(y,n)$ satisfying the first of these conditions, the only possible $\phi(y,n)$ from the full set of curves (Figure 3(a)) to satisfy the second is the constant profile, $\phi(y,n) = \phi(y) = \phi_c$, where the value ϕ_c must correspond to the local channel inclination angle $\alpha(y)$ at position y. If ϕ is monotone decreasing in n (*settled* regime), then the net flux in y is negative (towards the center of the spiral). Likewise if ϕ is monotone increasing in n (*ridged* regime), the net flux is positive (away from the center of the spiral). Therefore, the only valid profile of ϕ that satisfies the steady state condition is either ϕ_c (constant in n), or zero, which allows us to to construct relatively simple solutions. Based on this simple argument, we deduce a form of steady-state solution such that

the cross-sectional domain is divided into two distinct regions at a critical position $y = y_c$: region A ($-1 \leq y < y_c$) and region B ($y_c < y \leq 1$). The region B consists entirely of the clear fluid ($\phi = 0$), while region A contains particles with the concentration given by $\phi(y, n) = \phi_c(\alpha(y))$.

Analogous to the clear fluid problem [7], the centripetal component in the y-direction causes a clockwise secondary flow in the cross-section, in addition to the dominant flow in the axial direction. The coupling of the secondary flow with the particle equilibration in the n-direction indicates that the stable steady-state solution has the particles concentrated towards the center of the spiral, as illustrated in Figure 4(b). Perturbation of this arrangement by the secondary flow will carry particles near the free surface into the clear-fluid region, where they will quickly settle to the channel bottom due to the decrease in the volume fraction and the inclination angle, as indicated in the phase diagram (Figure 3(b)). Once the particles settle to the channel bottom, they are carried back towards the center by the secondary flow, which restores the equilibrium state. Should the particles be concentrated in the outer region of the spiral, as in Figure 4(c), perturbation by the secondary flow will carry particles near the bottom of the channel towards the center of the spiral. Although the local inclination angle increases in this direction, the large decrease in total volume fraction means that settling dominates, so that these particles remain near the bottom of the channel and are transported to the spiral center by the secondary flow. At the same time, due to the resultant decrease in the particle volume fraction (*i.e.* $\phi_0 < \phi_c$), the outer particle-laden region must become "settled" and, progressively, all the particles will move to the central region of the spiral. Therefore, the configuration of Figure 4(c) is unstable.

Overall, the particle profile in the normal direction is set by the dominant flow along the channel, which is equivalent to the incline problem. However, the secondary flow, which is unique to the spiral geometry, leads to particle segregation in the lateral direction. Specifically, the direction of the secondary flow causes the particles to move to the central region of the spiral.

A. Region A (particle-rich): $-1 \leq y < y_c$

In the inner region A containing the particulate material, the particles are assumed to have saturated at the critical volume fraction $\phi_c(\alpha(y))$, so that ϕ no longer varies with n

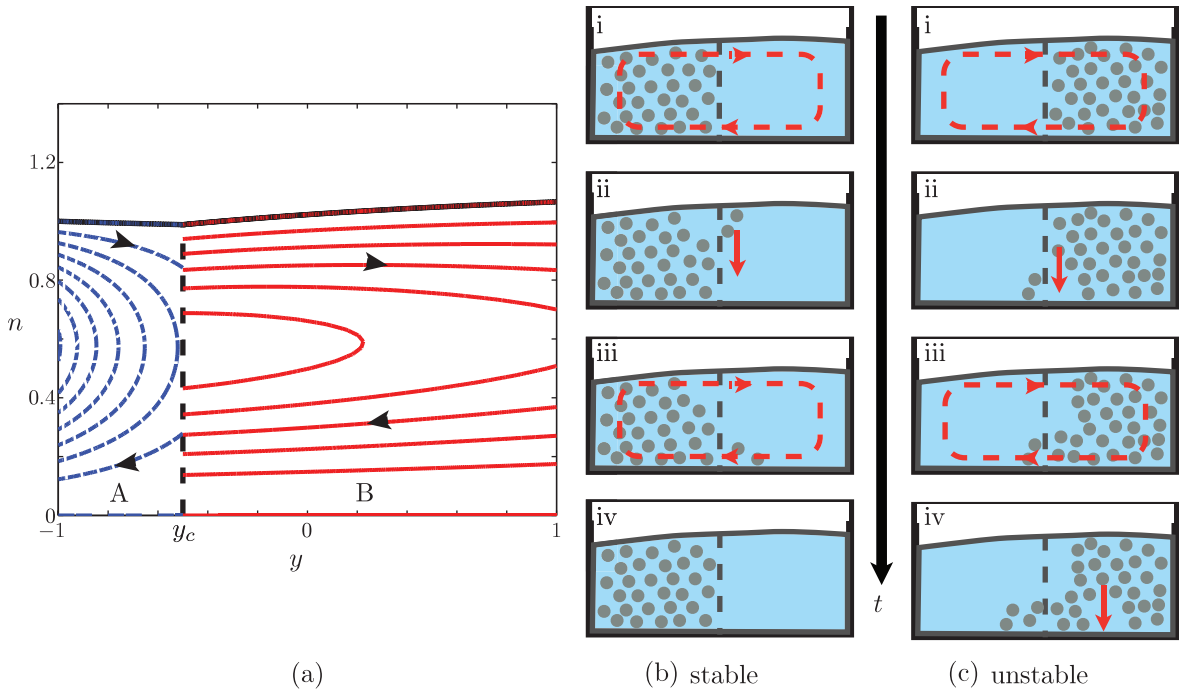

FIG. 4: **(a)** The streamlines of the particle-laden flow are computed for $\lambda = \epsilon = 0.29$. The cross-section is divided into two regions: region A (dotted lines) denotes the particle-rich region, while region B (solid lines) consists only of a clear fluid. The arrows indicate the presence of the clockwise secondary flow. Two equilibrium configurations are depicted in **(b)** and **(c)**, along with their time evolution, from top (i) to bottom (iv), as a result of perturbation by the secondary flow. The configuration in (b) is stable, while that in (c) is unstable.

and, thereby, satisfies the steady state condition. Thus, the expression for $\phi_c(y)$ can be obtained by setting $\partial\phi/\partial n = 0$ in Eq. (8) and combining it with Eq. (7c):

$$\phi_c(y) = \min\left[\sqrt{\left(\frac{1}{2\rho_s} + \frac{1+\epsilon y}{9\lambda K_c}\right)^2 + \frac{2(1+\epsilon y)}{9\lambda K_c}} - \left(\frac{1}{2\rho_s} + \frac{1+\epsilon y}{9\lambda K_c}\right), \phi_{\mathrm{m}}\right], \tag{9}$$

which monotonically increases in y until it reaches $\phi_{\mathrm{m}} = 0.61$, as shown in Figure 5(a) for channels with slope λ ranging from 0.22 to 0.35, and with $\epsilon = \lambda$. This is consistent with the fact that the local inclination angle, $\alpha = \arcsin(\lambda/(1+\epsilon y))$, decreases with y. As seen on the phase diagram in Figure 3(b), the critical volume fraction ϕ_c increases with decreasing α. Therefore, ϕ_c increases with y, or away from the spiral center.

This sets the present problem apart from the straight incline problem in which the inclination angle α is fixed for the entire channel width. The dependence of α on y was not

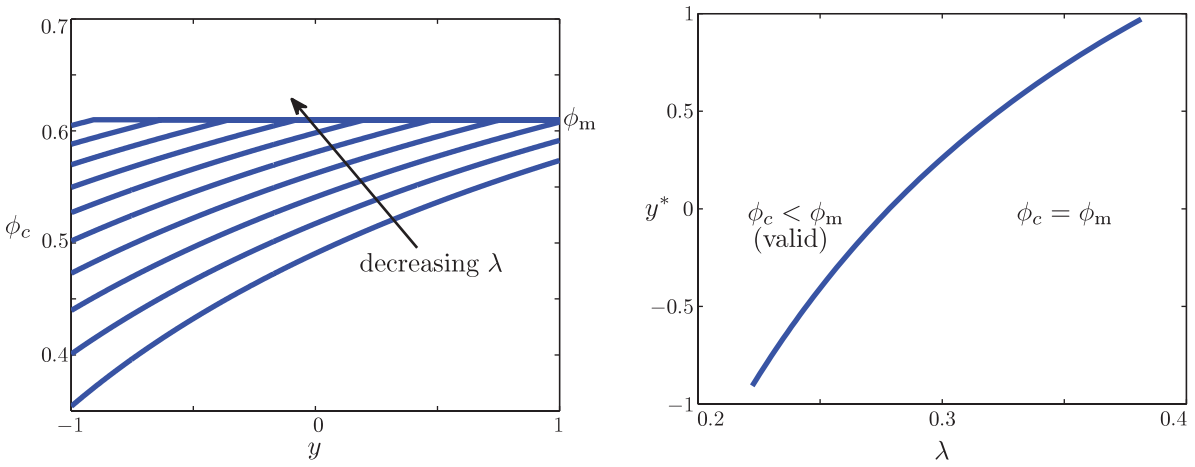

FIG. 5: **(a)** The critical volume fraction ϕ_c (constant in $\widetilde{n}$) is plotted as a function of y for $\epsilon = \lambda$ and $\lambda = [0.22, 0.24, 0.26, 0.29, 0.32, 0.35, 0.40, 0.46, 0.55, 0.67]$. **(b)** Our empirical model is valid for $\phi_c < \phi_m$, and ϕ_c increases to the maximum volume fraction ϕ_m for increasing y because the inclination angle $\alpha(y)$ decreases with y. For $\epsilon = \lambda$, we calculate the position $y^*(\lambda)$ above which ϕ_c is equal to ϕ_m. Accordingly, we must limit our parameter regime such that $y_c < y^*(\lambda)$ for the given spiral geometry.

included in the preliminary work [19] and is the result of the careful re-derivation of the governing equations in the helical coordinate system described in Section II. For given slope λ and curvature ϵ of the channel axis, ϕ_c must saturate to ϕ_m at a critical position $y = y^*$, which can be computed by setting $\phi_c = \phi_m$ in Eq. (9). The resultant value of y^* is plotted as a function of λ with $\epsilon = \lambda$ in Figure 5(b). For our empirical particle flux model to be valid, we must have $y_c < y^*$.

With $\phi_c(y)$ known, we next obtain expressions for the pressure and the components of the velocity in region A, in terms of the free surface profile $h(y)$. Integrating Eq. (7c) twice yields the downstream velocity,

$$u(y,n) = \frac{\kappa\lambda}{2\nu(1+\epsilon y)} n\left(2h(y) - n\right), \tag{10}$$

where $\nu = \mu/\rho = (\rho_s\phi_c + 1)^{-1}(1 - (\phi_c/\phi_m))^{-2}$ is also an explicit function of y, as the dependence of ϕ_c on y is known. Integrating Eq. (7b) gives the pressure, p:

$$p(y,n) = \rho\kappa\left(h(y) - n\right). \tag{11}$$

These expressions for u and p are then substituted into (7d). The term $\epsilon\lambda\sigma/(1+\epsilon y)^2$ in (7d) is neglected on the assumption that it is of order $\lambda^2 \ll 1$, but we retain the centripetal force term $\rho\chi u^2/(1+\epsilon y)$ on the assumption that it is of order one. We will examine the validity of these assumptions later, in Subsection C. We can now solve for v by integrating Eq. (7d) twice:

$$v(y,n) = \frac{\kappa}{2\nu}\left[\frac{dh}{dy}n\,(n-2h) + \frac{1}{\rho}\frac{d\rho}{dy}n\left(hn - h^2 - \frac{n^2}{3}\right)\right] \qquad (12)$$
$$- \frac{\kappa^2\widetilde{\chi}}{120\nu^3(1+\epsilon y)^3}n\left(n^5 - 6hn^4 + 10h^2n^3 - 16h^5\right),$$

where $\widetilde{\chi} \equiv \lambda^2\chi$. As in Stokes et al. [7], the integral form of the continuity equation, $\int_0^{h(y)} v(y,n)\,dn = 0$, yields

$$\frac{dh}{dy} = -\frac{3h}{8\rho}\frac{d\rho}{dy} + \frac{6\kappa\widetilde{\chi}h^4}{35\nu^2(1+\epsilon y)^3}, \qquad (13)$$

which is solved numerically for $h(y)$ for a given fluid depth at the left boundary $y=-1$ of the channel, $h(-1) = h_\ell$. For this we use a built-in ODE solver in MATLAB.

With the free surface profile determined, the pressure and velocity components may be computed. We may also compute the streamfunction ψ, by integrating $\partial\psi/\partial n = (1+\epsilon y)v$ subject to $\psi(n=h) = 0$, to obtain

$$\psi(y,n) = -(1+\epsilon y)\frac{\kappa}{48\mu}\frac{d\rho}{\partial y}n^2(2n-3h)(n-h) \qquad (14)$$
$$+ \frac{\kappa^2\widetilde{\chi}}{840\nu^3(1+\epsilon y)^2}n^2(2h-n)^2(h-n)\left[(h-z)^2 - 5h^2)\right].$$

These expressions for u, v, p, ψ, and the ODE for $h(y)$ differ from those in Stokes et al. [7], in that the fluid properties ν and ρ are functions of ϕ which is a function of y, and because the local channel angle is also a function of y, specifically $\sin\alpha(y) = \lambda/(1+\epsilon y)$.

B. Region B (clear fluid): $y_c < y \leq 1$

Velocity profiles and the pressure field in the clear-fluid region B are readily derived by setting $\rho = \nu = 1$ and $d\rho/dy = 0$ in the equations obtained for region A:

$$u(y,n) = \frac{\kappa\lambda}{2(1+\epsilon y)} n\left(2h(y) - n\right), \tag{15a}$$

$$p(y,n) = \kappa\left(h(y) - n\right), \tag{15b}$$

$$v(y,n) = \frac{\kappa}{2}\frac{dh}{dy} n\left(n - 2h\right) - \frac{\kappa^2\widetilde{\chi}}{120(1+\epsilon y)^3} n\left(n^5 - 6hn^4 + 10h^2n^3 - 16h^5\right). \tag{15c}$$

Similarly, the continuity condition ($\int_0^{h(y)} v(y,n)dn = 0$) leads to

$$\frac{dh}{dy} = \frac{6\kappa\widetilde{\chi}h^4}{35(1+\epsilon y)^3}, \tag{16}$$

which can be easily integrated to yield an analytic expression for the free surface profile h in region B:

$$h(y)^{-3} = h_c^{-3} + \frac{9\kappa\widetilde{\chi}}{35\epsilon}\left[(1+\epsilon y)^{-2} - (1+\epsilon y_c)^{-2}\right], \tag{17}$$

where $h_c = h(y_c)$ is the fluid depth at the boundary between regions A and B, $y = y_c$. We assume that the free surface is continuous at this boundary and determine h_c by matching to the free surface height in region A at $y = y_c$. In addition, the streamfunction ψ in region B is given by

$$\psi(y,n) = \frac{\kappa^2\widetilde{\chi}}{840(1+\epsilon y)^2} n^2(2h-n)^2(h-n)\left[(h-z)^2 - 5h^2)\right]. \tag{18}$$

C. Complete steady state solution

The complete steady state solutions have been determined using the following physical parameters: $U_0 = 0.1\,\mathrm{m/s}$, $a = 0.2\,\mathrm{m}$, $\nu_\ell = 5\times10^{-5}\mathrm{m}^2/\mathrm{s}$, $\rho_p/\rho_\ell = 2.5$, $K_v = 0.62$, $K_c = 0.41$, $d/H = 0.1$ and $\delta = H/a = 0.008$, which yield $Re = 400$, $Fr = 0.07$ and $\kappa = 5.2$. The parameters that pertain to particle properties are based on the particle-laden experiments on the straight incline [14]. With these parameters, the term that was neglected in (7d), namely $\epsilon\lambda\sigma/(1+\epsilon y)^2$, has magnitude $\epsilon\kappa\lambda^2 \approx 5\epsilon\lambda^2 \sim O(\lambda^2)$, which justifies its neglect, while the centripetal-force term which we retained has magnitude $\chi(\kappa\lambda/2)^2 = \epsilon\delta Re(\kappa\lambda/2)^2 \approx 20\epsilon\lambda^2$

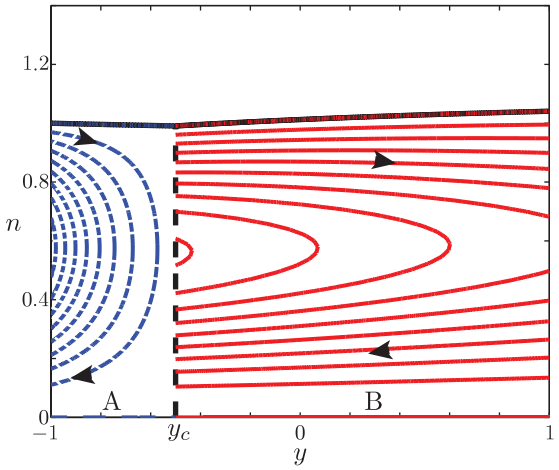

(a)

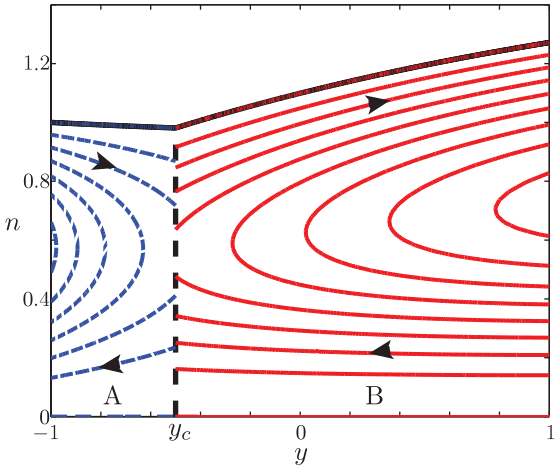

(b)

FIG. 6: The plots of streamlines for **(a)** $\lambda = \epsilon = 0.25$ and **(b)** $\lambda = \epsilon = 0.4$ Increasing the curvature ϵ and the inclination angle λ of the channel axis clearly results in an increase in fluid depth with distance from the vertical helix axis.

The particle Reynolds number is $Re_p = U_0 d/\nu_\ell = 0.3$, so that we neglect particle inertia at present. The dimensionless total mixture flux Q and total particle flux Q_p are easily determined once the free surface height $h(y)$ and the axial velocity $u(y, n)$ are known:

$$Q = \int_{-1}^{1} \int_{0}^{h(y)} u(y, n)\, dndy, \quad Q_\mathrm{p} = \int_{-1}^{y_c} \int_{0}^{h(y)} \phi_c(y) u(y, n)\, dndy. \tag{19}$$

Unique values of the parameters h_ℓ and y_c may be determined for specified values of the fluxes Q and Q_p.

We illustrate three steady solutions here for different values of the slope λ while $\epsilon = \lambda$, and for values of Q and Q_p such that $h_\ell = 1$ and $y_c = -0.5$. The streamlines in Figure 4(a) are for $\lambda = \epsilon = 0.29\,(\lambda^2 = 0.08)$, with corresponding values $Q = 0.66$ and $Q_p = 9.4 \times 10^{-4}$. Figure 6 gives streamline plots for $\lambda = \epsilon = 0.25$ and $\lambda = \epsilon = 0.4$ and illustrates the effect of increasing the slope λ and curvature ϵ together. The case $\lambda = \epsilon = 0.25$ ($Q = 0.55$, $Q_p = 1.8 \times 10^{-4}$) is quite similar to the case $\lambda = \epsilon = 0.29$ of Figure 4(a), with a free surface that is close to flat, while the case $\lambda = \epsilon = 0.4$ ($Q = 1.22$, $Q_p = 7.2 \times 10^{-3}$) more clearly shows a free surface that, in the particle-laden region, decreases in height with distance from the vertical axis of the helix, and then increases in height with distance from the vertical axis across the clear-fluid region.

V. DISCUSSION

In this paper, we have developed and examined a particle-laden flow model in a channel of rectangular cross section wound helically around a vertical axis. Our work has been inspired by a desire to understand the physics of spiral particle separators. In the steady state limit, we have shown that there exists a hydrodynamic segregation mechanism in the spiral geometry that is not seen in straight inclined channels. The curvature of the channel results in a separation of the particles from the fluid phase, with a particle-rich region near the spiral center and a clear fluid region away from the center.

To derive an equilibrium model, we reduced the governing equations by introducing two small parameters, namely small film thickness and small slope at the channel axis. In these limits, the effect of inertia comes in through the centripetal term in the momentum equation of the particle-fluid mixture. To model the coupling between the particles and the fluid flow, we have used a phenomenological model of particle-laden flow on an inclined plane [12, 14, 15]. This empirical model accounts for the interplay of particle settling due to gravity and shear-induced migration that opposes settling. As in Murisic et al. [15], we have scaled the particle diameter to the film thickness appropriately for the rapid equilibration of particles in the direction normal to the bottom of the channel. We have assumed the flow to be time-independent and helically symmetric, so that it is independent of axial position

along the channel. This physically corresponds to particle-laden flow down a spiral channel after it has undergone a sufficient number of turns to reach a steady state, with a constant flux of particles and fluid at the inlet.

The current theoretical model suggests that there exists a segregation mechanism that drives the particles towards the inside of the spiral. On a rapid timescale, the particles locally arrange themselves in the film thickness under the effects of gravity and shear flow. Since there must be zero net flux of particles and fluid in the transverse direction, the particle volume fraction must be constant in the direction normal to the bottom of the channel. While the secondary flow acts on the particles to carry them out of their equilibrium configuration, these perturbed particles settle on a short timescale and the original configuration is restored. Thus, the clockwise secondary flow due to the curvature of the helix ensures that the particles must saturate towards the center of the spiral in the steady state.

By applying the well-validated theoretical results of particle-laden flows to a spiral geometry, we have obtained an interesting result that the particles must concentrate towards the spiral center. This matches industrial observations for heavy particles and is the first mathematical model of particle-laden flow in helically-wound channels to include the coupling between the fluid and particles. Another point of interest that we here note is that, while the particle-laden region is adjacent to the spiral center, the theory shows the volume fraction of particles within this region to increase radially away from the spiral center, in the direction of decreasing local channel inclination. Experimental validation of the current theory will be the subject of future work. To understand the segregation of particles of different sizes and/or densities in spiral separators, we must consider polydisperse slurries. To that end, Lee et al. [23] have recently conducted experiments of bidisperse slurries down an incline, with the intention of applying these results to a spiral geometry. Lubrication models built on the equilibrium theory recently showed promise in describing the dynamic problem on a planar slope [24, 25] and can be extended to the current spiral geometry. Inclusion of particle inertia is also of interest, as spiral separators may be operated in the fast, inertia-dominated flow regime. These matters will be taken up in future work, with the ultimate aim of developing our understanding of the physics to give a sound theoretical basis for design and optimization of spiral separation for mineral processing and other industrial applications.

Acknowledgments

This work was supported by UC Lab Fees Research Grant 09-LR-04-116741-BERA and NSF grants DMS-1048840 and DMS-1312543. In addition, partial support of two visits by YMS to UCLA was provided by the University of Adelaide Special Studies Program.

APPENDIX: DERIVATION OF EQUATIONS

To derive our model we used the non-orthogonal coordinate system employed by Manoussaki and Chadwick [21] for an inviscid fluid-flow problem. Since ours is a viscous flow problem with a free surface and fluid properties that depend on spatial position, we here summarize the derivation of the full Navier-Stokes equations, along with the particle transport model used in this paper. We then obtain the governing equations in orthogonal coordinate directions suitable for approximation on the assumption that the fluid depth in the direction normal to the channel bottom is small relative to the channel half-width. For a detailed description of the tensor calculus required, see, for example, Simmonds [26].

1. Helical coordinates and basis vectors

For a right-hand helical channel of pitch $2\pi P$, the position $\mathbf{x}$ of a fluid element in the channel is defined by the coordinates $(\beta, r, z) \equiv (x^1, x^2, x^3)$ (see Figure 2) as

$$\mathbf{x}(\beta, r, z) = r\cos\beta\,\mathbf{i} + r\sin\beta\,\mathbf{j} + (P\beta + z)\,\mathbf{k}. \tag{A.1}$$

The basis vectors are [26], then, $\mathbf{e}_i = \partial\mathbf{x}/\partial x^i$, i.e.

$$\mathbf{e}_1 = \frac{\partial\mathbf{x}}{\partial\beta} = -r\sin\beta\,\mathbf{i} + r\cos\beta\,\mathbf{j} + P\,\mathbf{k}, \tag{A.2a}$$

$$\mathbf{e}_2 = \frac{\partial\mathbf{x}}{\partial r} = \cos\beta\,\mathbf{i} + \sin\beta\,\mathbf{j}, \tag{A.2b}$$

$$\mathbf{e}_3 = \frac{\partial\mathbf{x}}{\partial z} = \mathbf{k}, \tag{A.2c}$$

which are neither orthogonal nor all unit vectors. The corresponding dual basis vectors $\mathbf{e}^i$, such that $\mathbf{e}_i \cdot \mathbf{e}^j = \mathbf{e}^i \cdot \mathbf{e}_j = \delta_{ij}$ (the Kronecker delta), are

$$\mathbf{e}^1 = \frac{1}{r}(-\sin\beta\,\mathbf{i} + \cos\beta\,\mathbf{j}), \tag{A.3a}$$

$$\mathbf{e}^2 = \cos\beta\,\mathbf{i} + \sin\beta\,\mathbf{j}, \tag{A.3b}$$

$$\mathbf{e}^3 = \frac{P}{r}(\sin\beta\,\mathbf{i} - \cos\beta\,\mathbf{j}) + \mathbf{k}. \tag{A.3c}$$

Using Einstein summation notation we may write $\mathbf{e}^i = g^{ij}\mathbf{e}_j$, where $g^{ij} = \mathbf{e}^i \cdot \mathbf{e}^j$. Defining $\Lambda(r) = P/r$ and $\Upsilon(r) = 1 + P^2/r^2 = 1 + \Lambda^2$, the non-zero quantities g^{ij} are

$$g^{11} = \frac{1}{r^2}, \quad g^{22} = 1, \quad g^{33} = \Upsilon, \quad g^{13} = g^{31} = -\frac{\Lambda}{r}. \tag{A.4a}$$

Also, $\mathbf{e}_i = g_{ij}\mathbf{e}^j$, where $g_{ij} = \mathbf{e}_i \cdot \mathbf{e}_j$ and the non-zero quantities are

$$g_{11} = r^2\Upsilon, \quad g_{22} = 1, \quad g_{33} = 1, \quad g_{13} = g_{31} = r\Lambda. \tag{A.4b}$$

The velocity vector $\mathbf{u}$ is given by

$$\mathbf{u} = u^i\mathbf{e}_i = (|\mathbf{e}_i|u^i)\frac{\mathbf{e}_i}{|\mathbf{e}_i|} = u^{(i)}\hat{\mathbf{e}}_i \tag{A.5a}$$

where $|\mathbf{e}_i| = \sqrt{g_{ii}}$ and $|\mathbf{e}_i|u^i = u^{(i)}$ are the physical components of velocity in the directions of the unit vectors $\hat{\mathbf{e}}_i = \mathbf{e}_i/|\mathbf{e}_i|$. Hence, the physical vector quantities are

$$u^{(1)} = (r\sqrt{\Upsilon})u^1, \quad u^{(2)} = u^2, \quad u^{(3)} = u^3. \tag{A.5b}$$

Similarly, the particle flux vector is

$$\mathbf{J} = J^i\mathbf{e}_i = J^{(i)}\hat{\mathbf{e}}_i \quad \text{with} \quad J^{(1)} = (r\sqrt{\Upsilon})J^1, \quad J^{(2)} = J^2, \quad J^{(3)} = J^3. \tag{A.6}$$

2. The helically-symmetric equations

To write down the helically-symmetric equations in this non-orthogonal helical coordinate system, we use the following vector operations, written in terms of the scalar pressure function $p(\beta, r, z) = p(x^i)$ and the vector velocity $\mathbf{u}(\beta, r, z) = u^i(x^j)$ and where Einstein summation notation has been used:

$$\boldsymbol{\nabla} p = \mathbf{e}^i\frac{\partial p}{\partial x^i} = \frac{\partial p}{\partial x^i}g^{ij}\mathbf{e}_j, \tag{A.7a}$$

$$\mathbf{u}\cdot\boldsymbol{\nabla}p = u^i\frac{\partial p}{\partial x^i}, \tag{A.7b}$$

$$\boldsymbol{\nabla}\cdot\mathbf{u} = \frac{\partial u^i}{\partial x^i} + u^j\Gamma^i_{ij}, \tag{A.7c}$$

$$(\mathbf{u}\cdot\boldsymbol{\nabla})\mathbf{u} = \left(u^j\frac{\partial u^i}{\partial x^j} + u^j u^k\Gamma^i_{kj}\right)\mathbf{e}_i, \tag{A.7d}$$

$$\boldsymbol{\nabla}\mathbf{u} = \mathcal{U}^{ij} = \left(\frac{\partial u^j}{\partial x^k} + u^m\Gamma^j_{mk}\right)g^{ik}, \tag{A.7e}$$

$$\boldsymbol{\nabla}\mathbf{u} + (\boldsymbol{\nabla}\mathbf{u})^T = \mathcal{S}^{ij} = \left(\frac{\partial u^j}{\partial x^k} + u^m\Gamma^j_{mk}\right)g^{ik} + \left(\frac{\partial u^i}{\partial x^k} + u^m\Gamma^i_{mk}\right)g^{jk}, \tag{A.7f}$$

$$\boldsymbol{\nabla}\cdot\mathcal{S} = \left(\frac{\partial S^{ji}}{\partial x^j} + S^{ji}\Gamma^k_{kj} + S^{kj}\Gamma^i_{kj}\right)\mathbf{e}_i. \tag{A.7g}$$

Here $\Gamma^k_{ij} = \Gamma^k_{ji}$ are the Christoffel symbols, defined by

$$\frac{\partial\mathbf{e}_i}{\partial x^j} = \Gamma^k_{ij}\mathbf{e}_k. \tag{A.7h}$$

For our helical coordinate system the only non-zero Christoffel symbols are

$$\Gamma^2_{11} = -r, \quad \Gamma^1_{12} = \frac{1}{r}, \quad \Gamma^3_{12} = -\Lambda. \tag{A.8}$$

Recall that for helical symmetry all quantities are independent of angle β. Note also that, from here on, we have used the notation

$$u^j_{,i} \equiv \frac{\partial u^j}{\partial x^i} \tag{A.9}$$

and, for clarity, substituted the appropriate variable for subscript and superscript indices; $u^j_{,t}$ denotes the time derivative of velocity component u^j.

The continuity equation for an incompressible fluid is, simply,

$$\frac{1}{r}(ru^r)_{,r} + u^z_{,z} = 0 \quad \text{or} \quad u^r_{,r} + \frac{u^r}{r} + u^z_{,z} = 0, \tag{A.10}$$

which permits definition of the streamfunction ψ, such that

$$\psi_{,r} = ru^z, \quad -\psi_{,z} = ru^r. \tag{A.11}$$

In writing down the Navier-Stokes equations for a Newtonian incompressible fluid, we have used the continuity equation to remove mixed derivatives from the divergence of the stress tensor.

The Navier-Stokes equations are then, in the coordinate direction $\mathbf{e}_1 = \mathbf{e}_\beta$,

$$\rho\left(u^\beta_{,t} + u^r u^\beta_{,r} + u^z u^\beta_{,z} + \frac{2}{r}u^r u^\beta\right) = \frac{\Lambda}{r}p_{,z} + \mu\left(u^\beta_{,rr} + \Upsilon u^\beta_{,zz} + \frac{3}{r}u^\beta_{,r} - \frac{2\Lambda}{r^2}u^r_{,z}\right) + \mu_{,r}\left(-\frac{\Lambda}{r}u^r_{,z} + u^\beta_{,r}\right) + \mu_{,z}\left(-\frac{2\Lambda u^r}{r^2} + \Upsilon u^\beta_{,z} - \frac{\Lambda}{r}u^z_{,z}\right), \tag{A.12a}$$

in the coordinate direction $\mathbf{e}_2 = \mathbf{e}_r$,

$$\rho\left(u^r_{,t} + u^r u^r_{,r} + u^z u^r_{,z} - r u^\beta u^\beta\right) = -p_{,r} + \mu\left(u^r_{,rr} + \Upsilon u^r_{,zz} + \frac{1}{r}\left(u^r_{,r} - \frac{u^r}{r}\right) + 2\Lambda u^\beta_{,z}\right) + 2\mu_{,r}u^r_{,r} + \mu_{,z}\left(\Upsilon u^r_{,z} + u^z_{,r}\right), \tag{A.12b}$$

and in the coordinate direction $\mathbf{e}_3 = \mathbf{e}_z$,

$$\rho\left(u^z_{,t} + u^r u^z_{,r} + u^z u^z_{,z} - 2\Lambda u^r u^\beta\right) = -\Upsilon p_{,z} + \mu\left(u^z_{,rr} + \Upsilon u^z_{,zz} + \frac{2\Lambda^2}{r}u^r_{,z} + \frac{1}{r}u^z_{,r} - 2\Lambda u^\beta_{,r}\right) + \mu_{,r}\left(\Upsilon u^r_{,z} + u^z_{,r}\right) + 2\mu_{,z}\left(\frac{\Lambda^2}{r}u^r + \Upsilon u^z_{,z}\right) - \rho g. \tag{A.12c}$$

The particle transport equation for a general particle flux vector $\mathbf{J} = (J^\beta, J^r, J^z)$ is

$$\phi_{,t} + u^r\phi_{,r} + u^z\phi_{,z} + J^r_{,r} + \frac{1}{r}J^r + J^z_{,z} = 0, \tag{A.13a}$$

while the components of the particle flux vector (5) used in this paper are

$$J^\beta = -\frac{K_c d^2}{4}\phi r\Lambda(\dot\gamma\phi)_{,z} - \frac{K_v d^2}{4}\frac{\phi^2\dot\gamma}{\mu(\phi)}\frac{d\mu}{d\phi}r\Lambda\phi_{,z}, \tag{A.13b}$$

$$J^r = -\frac{K_c d^2}{4}\phi(\dot\gamma\phi)_{,r} - \frac{K_v d^2}{4}\frac{\phi^2\dot\gamma}{\mu}\frac{d\mu}{d\phi}\phi_{,r}, \tag{A.13c}$$

$$J^z = \frac{d^2\phi(\rho_p - \rho_\ell)}{18\mu}(1-\phi)g - \frac{K_c d^2}{4}\phi\Upsilon(\dot\gamma\phi)_{,z} - \frac{K_v d^2}{4}\frac{\phi^2\dot\gamma}{\mu}\frac{d\mu}{d\phi}\Upsilon\phi_{,z}. \tag{A.13d}$$

3. Boundary conditions

The boundary conditions for the fluid flow problem considered in this paper are no slip on channel walls and, neglecting surface tension, zero normal and tangential stresses on the free surface. The zero stress conditions are

$$(\mu\mathcal{S}^{ij} - pg^{ij})n_j = 0,\ i = 1,2,3, \tag{A.14}$$

where $\mathbf{n}$ is a vector normal to the free surface. For a free surface $F(r,z) = 0$, which is independent of β because of helical symmetry, this normal is given by

$$\mathbf{n} = \nabla F = n_i\mathbf{e}^i, \quad n_i = \frac{\partial F}{\partial x^i}. \tag{A.15}$$

Writing out the components of (A.14) gives

$$F_{,r}\left(-\frac{\mu\Lambda}{r}u^r_{,z}+\mu u^\beta_{,r}\right)+F_{,z}\left(\frac{\Lambda}{r}p-\frac{2\mu\Lambda}{r^2}u^r+\mu\Upsilon u^\beta_{,z}-\frac{\mu\Lambda}{r}u^z_{,z}\right)=0, \tag{A.16a}$$

$$F_{,r}\left(-p+2\mu u^r_{,r}\right)+F_{,z}\left(\mu\Upsilon u^r_{,z}+\mu u^z_{,r}\right)=0, \tag{A.16b}$$

$$F_{,r}\left(\mu\Upsilon u^r_{,z}+\mu u^z_{,r}\right)+F_{,z}\left(-\Upsilon p+\frac{2\mu\Lambda^2}{r}u^r+2\mu\Upsilon u^z_{,z}\right)=0. \tag{A.16c}$$

The boundary conditions accompanying the particle transport equation are zero normal particle flux at the channel wall $z=0$ and at the free surface $F(r,z)=0$. Thus, we have

$$J^z=0 \quad \text{on } z=0, \tag{A.17a}$$

$$J^rF_{,r}+J^zF_{,z}=0 \quad \text{on } F(r,z)=0. \tag{A.17b}$$

4. Model equations in orthogonal coordinate directions

Finally, we obtain the model equations in the three orthogonal directions

$$\hat{\mathbf{e}}_\beta=\frac{\mathbf{e}_\beta}{|\mathbf{e}_\beta|}=\frac{1}{\sqrt{\Upsilon}}(-\sin\beta\mathbf{i}+\cos\beta\mathbf{j}+\Lambda\mathbf{k}), \tag{A.18a}$$

$$\hat{\mathbf{e}}_r=\mathbf{e}_r=\cos\beta\mathbf{i}+\sin\beta\mathbf{j}, \tag{A.18b}$$

$$\hat{\mathbf{e}}_n=\hat{\mathbf{e}}_r\times\hat{\mathbf{e}}_\beta=\frac{\Lambda}{\sqrt{\Upsilon}}\left(\sin\beta\mathbf{i}-\cos\beta\mathbf{j}+\frac{1}{\Lambda}\mathbf{k}\right). \tag{A.18c}$$

Because $\mathbf{e}_\beta$ and $\mathbf{e}_z$ are not orthogonal vectors, the velocity component in the coordinate direction $\mathbf{e}_z$ includes a component that is in the coordinate direction $\mathbf{e}_\beta$. We have

$$\mathbf{e}_z=\mathbf{k}=\frac{1}{\sqrt{\Upsilon}}(\Lambda\hat{\mathbf{e}}_\beta+\hat{\mathbf{e}}_n)=\frac{\Lambda}{r\Upsilon}\mathbf{e}_\beta+\frac{1}{\sqrt{\Upsilon}}\hat{\mathbf{e}}_n, \tag{A.19}$$

and

$$\mathbf{u}=u^{(\beta)}\hat{\mathbf{e}}_\beta+u^{(r)}\hat{\mathbf{e}}_r+u^{(z)}\frac{1}{\sqrt{\Upsilon}}(\Lambda\hat{\mathbf{e}}_\beta+\hat{\mathbf{e}}_n)=\left(u^{(\beta)}+\frac{\Lambda}{\sqrt{\Upsilon}}u^{(z)}\right)\hat{\mathbf{e}}_\beta+u^{(r)}\hat{\mathbf{e}}_r+\frac{1}{\sqrt{\Upsilon}}u^{(z)}\hat{\mathbf{e}}_n, \tag{A.20}$$

where $u^{(r)}$, $u^{(\beta)}$ and $u^{(z)}$ are as defined in (A.5b) but with index numbers replaced by variables. We now define the physical velocity components

$$v^\beta=u^{(\beta)}+\frac{\Lambda}{\sqrt{\Upsilon}}u^{(z)}=r\sqrt{\Upsilon}u^\beta+\frac{\Lambda}{\sqrt{\Upsilon}}u^z, \quad v^r=u^{(r)}=u^r, \quad v^n=\frac{1}{\sqrt{\Upsilon}}u^{(z)}=\frac{1}{\sqrt{\Upsilon}}u^z, \tag{A.21}$$

such that $\mathbf{u}=v^\beta\hat{\mathbf{e}}_\beta+v^r\hat{\mathbf{e}}_r+v^n\hat{\mathbf{e}}_n$. Then

$$u^\beta=\frac{1}{r\sqrt{\Upsilon}}(v^\beta-\Lambda v^n) \quad \text{and} \quad u^z=\sqrt{\Upsilon}v^n. \tag{A.22}$$

Next we write (A.10) and (A.12b)–(A.12c) in terms of v^r, v^β and v^n, and move the $\hat{\mathbf{e}}_\beta$ component of (A.12c) to (A.12a), to obtain the fluid flow equations in the orthogonal $\hat{\mathbf{e}}_r$, $\hat{\mathbf{e}}_\beta$, $\hat{\mathbf{e}}_n$ directions. Defining $n = z/\sqrt{\Upsilon}$ to be the coordinate in direction $\hat{\mathbf{e}}_n$, we also have

$$\frac{\partial}{\partial z} = \frac{1}{\sqrt{\Upsilon}}\frac{\partial}{\partial n} \quad \text{or} \quad \sqrt{\Upsilon}\frac{\partial}{\partial z} = \frac{\partial}{\partial n}. \tag{A.23}$$

Using Maple, we find that the continuity equation is

$$\frac{1}{r}(rv^r)_{,r} + v^n_{,n} = 0 \quad \text{or} \quad v^r_{,r} + \frac{v^r}{r} + v^n_{,n} = 0, \tag{A.24a}$$

admitting the stream function defined by

$$\psi_{,r} = ru^n, \quad -\psi_{,n} = ru^r, \tag{A.24b}$$

while the Navier-Stokes equations are, in the coordinate direction $\hat{\mathbf{e}}_\beta$,

$$\begin{aligned}\rho\left(v_{,t} + v^r v^\beta_{,r} + v^n v^\beta_{,n} + \frac{1}{r\Upsilon}v^r v^\beta\right) &= \mu\left[v^\beta_{,rr} + v^\beta_{,nn} + \frac{1}{r}v^\beta_{,r} - \frac{2\Lambda}{r\Upsilon}\left(v^r_{,n} - v^n_{,r}\right)\right.\\ &\left. - \left(\frac{2\Upsilon - 1}{r^2\Upsilon^2}\right)v^\beta + \frac{2\Lambda(\Upsilon-1)}{r^2\Upsilon^2}v^n\right] + \mu_{,r}\left[v^\beta_{,r} - \frac{1}{r\Upsilon}\left(v^\beta - 2\Lambda v^n\right)\right]\\ &+ \mu_{,n}\left[-\frac{2\Lambda}{r\Upsilon}v^r + v^\beta_{,n}\right] - \frac{\Lambda}{\sqrt{\Upsilon}}\rho g,\end{aligned} \tag{A.24c}$$

in the coordinate direction $\hat{\mathbf{e}}_r$,

$$\begin{aligned}\rho\left[v^r_{,t} + v^r v^r_{,r} + v^n v^r_{,n} - \frac{1}{r\Upsilon}\left(v^\beta - \Lambda v^n\right)^2\right] &= -p_r + \mu\left[v^r_{,rr} + v^r_{,nn} + \frac{1}{r}\left(v^r_{,r} - \frac{v^r}{r}\right)\right.\\ &\left. + \frac{2\Lambda}{r\Upsilon}(v^\beta_{,n} - \Lambda v^n_{,n})\right] + 2\mu_{,r}v^r_{,r} + \mu_{,n}\left[v^r_{,n} + v^n_{,r} - \left(\frac{\Upsilon - 1}{r\Upsilon}\right)v^n\right],\end{aligned} \tag{A.24d}$$

and in the coordinate direction $\hat{\mathbf{e}}_n$,

$$\begin{aligned}\rho\left(v^n_{,t} + v^r v^n_{,r} + v^n v^n_{,n} - v^r\frac{\Lambda}{r\Upsilon}(2v^\beta - \Lambda v^n)\right) &= -p_n + \mu\left[v^n_{,rr} + v^n_{,nn} - \frac{2\Lambda}{r\Upsilon}\left(v^\beta_{,r} - \Lambda v^r_{,n}\right)\right.\\ &\left. + \frac{1}{r}\left(v^n_{,r} - \frac{v^n}{r}\right) + \frac{1}{r^2\Upsilon^2}\left(v^n + 2\Lambda v^\beta\right)\right] + \mu_{,r}\left[v^r_{,n} + v^n_{,r} - \frac{(\Upsilon-1)}{r\Upsilon}v^n\right]\\ &+ 2\mu_{,n}\left[\frac{(\Upsilon-1)}{r\Upsilon}v^r + v^n_{,n}\right] - \frac{\rho g}{\sqrt{\Upsilon}}.\end{aligned} \tag{A.24e}$$

In the (β, r, n) coordinates, the boundary conditions (A.16a)–(A.16c) are

$$\begin{aligned}F_{,r}\left(-\frac{\mu\Lambda}{r}v^r_{,n} + \mu\left[\frac{1}{r}v^\beta_{,r} - \frac{1}{\Upsilon r^2}v^\beta + \frac{\Lambda(1+\Upsilon)}{\Upsilon r^2}v^n - \frac{\Lambda}{r}\frac{\partial v^n}{\partial r}\right]\right)\\ + F_{,n}\left(\frac{\Lambda}{r}p - \frac{2\mu\Lambda}{r^2}v^r + \frac{\mu}{r}v^\beta_{,n} - \frac{2\mu\Lambda}{r}v^n_{,n}\right) = 0,\end{aligned} \tag{A.25a}$$

$$F_{,r}\left(-p+2\mu v^r_{,r}\right)+F_{,n}\left(\mu v^r_{,n}+\mu v^n_{,r}-\frac{\mu\Lambda^2}{r\Upsilon}v^n\right)=0, \tag{A.25b}$$

$$F_{,r}\left(\mu v^r_{,n}+\mu v^n_{,r}-\frac{\mu\Lambda^2}{r\Upsilon}v^n\right)+F_{,n}\left(-p+\frac{2\mu\Lambda^2}{r\Upsilon}v^r+2\mu v^n_{,n}\right)=0. \tag{A.25c}$$

Finally, we have the particle flux vector

$$\mathbf{J}=\left(J^{(\beta)}+\frac{\Lambda}{\sqrt{\Upsilon}}J^{(z)}\right)\hat{\mathbf{e}}_\beta+J^{(r)}\hat{\mathbf{e}}_r+\frac{1}{\sqrt{\Upsilon}}J^{(z)}\hat{\mathbf{e}}_n, \tag{A.26}$$

where $J^{(r)}$, $J^{(\beta)}$ and $J^{(z)}$ are as defined in (A.6), with index numbers replaced by variables. Then, in terms of physical components

$$J^{(r)}=J^r,\quad J^n=\frac{1}{\sqrt{\Upsilon}}J^{(z)}=\frac{1}{\sqrt{\Upsilon}}J^z, \tag{A.27}$$

(A.13a) may be written

$$\phi_{,t}+v^r\phi_{,r}+v^n\phi_{,n}+J^r_{,r}+\frac{1}{r}J^r+J^n_{,n}=0, \tag{A.28a}$$

with

$$J^r=-\frac{K_cd^2}{4}\phi(\dot\gamma\phi)_{,r}-\frac{K_vd^2}{4}\frac{\phi^2\dot\gamma}{\mu}\frac{d\mu}{d\phi}\phi_{,r}, \tag{A.28b}$$

$$J^n=\frac{d^2\phi(\rho_p-\rho_\ell)}{18\mu\sqrt{\Upsilon}}(1-\phi)g-\frac{K_cd^2}{4}\phi(\dot\gamma\phi)_{,n}-\frac{K_vd^2}{4}\frac{\phi^2\dot\gamma}{\mu}\frac{d\mu}{d\phi}\phi_{,n}, \tag{A.28c}$$

and the boundary conditions (A.17a) and (A.17b) become

$$J^n=0\quad\text{on } z=0, \tag{A.29a}$$

$$J^rF_{,r}+J^nF_{,n}=0\quad\text{on } F(r,n)=0. \tag{A.29b}$$

---

[1] B. Weldon. Fine coal beneficiation: spiral separators in the australian industry. *The Australian Coal Review*, pages 25–28, 11 1997.

[2] A. B. Holland-Batt and P. N. Holtham. Particle and fluid motion on spiral separators. *Minerals Engineering*, 4:457–482, 1991.

[3] W. R. Dean. The streamline motion of flow in a curved pipe. *Phil. Mag.*, 5:673–695, 1928.

[4] A. B. Holland-Batt. Spiral separation: theory and simulation. *Trans. Instn Min, Metall. (Sect C: Mineral Process. Extr. Metall.)*, 98:C46, 1989.

[5] P. N. Holtham. Flow visualisation of secondary currents on spiral separators. *Miner. Eng.*, 3:279–286, 1990.

[6] Y. M. Stokes, S. R. Wilson, and B. R. Duffy. Thin-film flow in open helically-wound channels. In M. Behnia, W. Lin, and G. D. McBain, editors, *15th Australian Fluid Mechanics Conference (CSROM)*. Paper AFMC00187, 2004.

[7] Y. M. Stokes, B. R. Duffy, S. R. Wilson, and H. Tronnolone. Thin-film flow in a helically wound rectangular channel with small torsion. *Phys. Fluids*, 25:083103, 2013.

[8] D. K. Das, K. M. Godiwalla, P. Lopamudra, K. K. Bhattacharya, R. Singh, and S. P. Mehrotra. Mathematical modeling of separation characteristics of a coal-washing spiral. *Int. J. Miner. Process.*, 84:118–132, 2007.

[9] R. A. Bagnold. Experiments on a gravity-free dispersion of large solid spheres in a newtonian fluid under shear. *Proc. R. Soc. Lond. A*, 225:49–63, 1954.

[10] B. W. Matthews, C. A. J. Fletcher, and A. C. Partridge. Computational simulation of fluid and diulte particulate flows on spiral concentrators. *Appl. Math. Model.*, 22:965–979, 1998.

[11] J. Zhou, B. Dupuy, A. L. Bertozzi, and A. E. Hosoi. Theory for shock dynamics in particle-laden thin films. *Phys. Rev. Lett.*, 94(11):117803, 2005.

[12] B. P. Cook. Theory for particle settling and shear-induced migration in thin-film liquid flow. *Phys. Rev. E.*, 78:045303, 2008.

[13] T. Ward, C. Wey, R. Glidden, A. E. Hosoi, and A. L. Bertozzi. Theory for shock dynamics in particle-laden thin films. *Phys. Fluids*, 21:083305, 2009.

[14] N. Murisic, J. Ho, V. Hu, P. Latterman, T. Koch, K. Lin, M. Mata, and A. L. Bertozzi. Particle-laden viscous thin-film flows on an incline: experiments compared with an equilibrium theory based on shear-induced migration and particle settling. *Physica D*, 240(20):1661–1673, 2011.

[15] N. Murisic, B. Pausader, D. Peschka, and A. L. Bertozzi. Dynamics of particle settling and resuspension in viscous liquid films. *J. Fluid Mech.*, 717:203–231, 1 2013.

[16] D. Leighton and A. Acrivos. The shear-induced migration of particles in concentrated suspensions. *J. Fluid Mech.*, 181:415–439, 1987.

[17] R. J. Phillips, R. C. Armstrong, R. A. Brown, A. L. Graham, and J. R. Abbott. A constitutive equation for concentrated suspensions that accounts for shear-induced particle migration. *Phys. Fluids*, 4(1):30–40, 1992.

[18] P. R. Nott and J. F. Brady. Pressure-driven flow of suspensions: simulation and theory. *J. Fluid Mech.*, 275:157–199, 8 1994.

[19] S. Lee, Y. M. Stokes, and A. L. Bertozzi. A model for particle laden flow in a spiral concentrator. In Y. Bai, J. Wang, and F. Daining, editors, *23rd International Congress of Theoretical and Applied Mechanics (ICTAM)*. Procedia IUTAM, 2012.

[20] M. Germano. The dean equations extended to a helical pipe flow. *J. Fluid Mech.*, 203:289–305, 1989.

[21] D. Manoussaki and R.S. Chadwick. Effects of geometry on fluid loading in a coiled cochlea. *SIAM J. Appl. Math.*, 61(2):369–386, 2000.

[22] B. P. Cook, A. L. Bertozzi, and A. E. Hosoi. Shock solutions for particle-laden thin films. *SIAM J. Appl. Math.*, 68(3):760–783, 2008.

[23] S. Lee, A. Mavromoustaki, G. Urdaneta, K. Huang, and A. L. Bertozzi. Experimental investigation of bidensity slurries on an incline. preprint.

[24] A. Mavromoustaki and A. L. Bertozzi. Hyperbolic systems of conservation laws in gravity-driven, particle-laden thin-film flows. submitted to J. Eng. Math. (2013).

[25] L. Wang and A. L. Bertozzi. Shock solutions for high concentration particle-laden thin films. submitted to SIAP (2013).

[26] J.G. Simmonds. *A brief on tensor analysis*. Springer, New York, 2 edition, 1994.